JOURNAL OF GEOPHYSICAL RESEARCH, VOL. 103, NO. B8, PAGES 17,901–17,918, AUGUST 10, 1998

A two-dimensional *P-SV* hybrid method and its application to modeling localized structures near the core-mantle boundary

Lianxing Wen and Donald V. Helmberger

Seismological Laboratory, California Institute of Technology, Pasadena

Abstract. A *P-SV* hybrid method is developed for calculating synthetic seismograms involving two-dimensional localized heterogeneous structures. The finite difference technique is applied in the heterogeneous region and generalized ray theory solutions from a seismic source are used in the finite difference initiation process. The seismic motions, after interacting with the heterogeneous structures, are propagated back to the Earth's surface analytically with the aid of the Kirchhoff method. Anomalous long-period *SKS-SPdKS* observations, sampling a region near the core-mantle boundary beneath the southwest Pacific, are modeled with the hybrid method. Localized structures just above the core-mantle boundary, with lateral dimensions of 250 to 400 km, can explain even the most anomalous data observed to date if *S* velocity drops up to 30% are allowed for a *P* velocity drop of 10%. Structural shapes and seismic properties of those anomalies are constrained from the data since synthetic waveforms are sensitive to the location and lateral dimension of seismic anomalies near the core-mantle boundary. Some important issues, such as the density change and roughness of the structures and the sharpness of the transition from the structures to the surrounding mantle, however, remain unresolved due to the nature of the data.

1. Introduction

The core-mantle boundary (CMB) and adjacent regions play a fundamental role in the mantle and core dynamics, and resolving the lateral variations of seismic structure in this region is crucial to understanding the region's thermal, chemical, and dynamical behavior. Many seismological observations have suggested the existence of small-scale heterogeneities in the lowermost mantle. For example, the decay rate of the diffracted *P* waves [*Alexander and Phinney*, 1966] and the precursors to *PKP* [*Cleary and Haddon*, 1972; *Cormier*, 1995] have been interpreted as results of scattering by seismic heterogeneities in the lowermost mantle, although the precise nature of those scatterers has not been known. *Doornbos* [1976, 1978, 1988] show that the topographic relief of the core-mantle boundary with scale lengths of about 10-20 km and an amplitude of several hundred meters offers an equally feasible explanation for the observed precursors to *PKP* phase. The complexities of *SKS* and *SPdKS* phases sampling non-circum-Pacific regions in the core-mantle boundary region have been interpreted in term of the presence of ultralow-velocity layers just above the core-mantle boundary, with a thickness of tens of kilometers [*Garnero et al.*, 1993; *Garnero and Helmberger*, 1995, 1996; *Helmberger et al.*, 1996]. The presence of a low seismic velocity layer is also invoked to explain the precursor to the *PcP* phase recorded in California from events in Fiji [*Mori and Helmberger*, 1995]. Rapid variation of waveforms of those phases from event to event strongly suggests that these structures rapidly vary with length scales which are very small compared to the length of the ray path.

Both numerical and analytical methods have difficulties in handling this type of wave propagation. Numerical methods (e.g., finite difference [*Alterman and Karal*, 1968; *Boore*, 1972; *Virieux*, 1984] and finite element [*Lysmer and Drake*, 1972]) require massive computer memory and have been limited to wave propagation at small distances and to low frequency modeling [e.g., *Igel and Weber*, 1996], even though they can handle wave propagation in heterogeneous media. Analytic methods (e.g., the generalized ray theory [*Helmberger*, 1968], the WKB method [*Chapman*, 1976] and the reflectivity method [*Müller*, 1985]), on the other hand, can only deal with one-dimensional models. Even though some modifications of these methods enable them to deal with wave propagation in dipping layered structures [*Hong and Helmberger*, 1978] or smooth boundary structures [*Helmberger et al.*, 1996; *Liu and Tromp*, 1996], these methods cannot be applied to wave propagation in strongly heterogeneous media.

In this paper, we combine advantages of both numerical and analytical methods and develop a hybrid

Paper number 98JB01276.
0148-0227/98/98JB-01276$09.00

method by applying a finite difference technique in heterogeneous regions and analytical methods outside. The generalized ray theory solutions are interfaced with the finite difference calculation and synthetic seismograms at the Earth's surface are obtained from interfacing the output of the finite difference calculation with WKB Green's functions using Kirchhoff theory. The staggered-grid finite difference scheme [*Virieux*, 1986] is used to handle the fluid-solid interface. We present the theory of hybrid method in section 2. As an application, in section 3, we show that the observed *SKS* and *SPdKS* phases sampling the core-mantle boundary region beneath the southwest Pacific can be explained with a simple dome-shaped structure just above the core-mantle boundary. We discuss the length scales of those seismic structures as well as the trade-offs among parameters: S velocity drop, curvature, geometry, roughness, and sharpness of the transition to the surrounding mantle.

2. A Two-Dimensional *P-SV* Hybrid Method Combining Generalized Ray Theory, Finite Difference, WKB, and Kirchhoff Theory

The *P-SV* wave propagation problem is illustrated in Figure 1a, where we assume the Earth flattening approximation. The heterogeneous region is bounded by a box, where a finite difference technique is applied. The generalized ray theory (GRT) solutions are interfaced with the finite difference (FD) calculation in the shaded regions in Figure 1b. The wave fields are output from the finite difference calculation just below the core-mantle boundary, which are indicated by open triangles. The solutions in solid triangles are calculated directly by the generalized ray theory, since those regions are affected very little by the presence of heterogeneities. The synthetics at the surface of the Earth are obtained by applying the Kirchhoff method to interface the output of receivers (triangles in Figure 1a) with WKB Green's functions. Interfacings of these motions are discussed in sections 2.1 and 2.2.

2.1. GRT-FD Interfacing

Shtivelman [1985] and *Emmerich* [1989] present one way to handle the interfacing between the finite difference technique and the analytical method by dividing the finite difference region into two regions. The situation is slightly different here. The left boundary requires special treatment as well.

The staggered-grid scheme is used for finite differencing the *P-SV* wave equations [*Virieux*, 1986; *Levander*, 1988]. Finite difference grids are illustrated in Figure 1b, where vertical and horizontal velocities are indicated by triangles and circles, and normal and shear stresses are represented by diamonds and squares. The finite difference grids are divided into three regions, separated by the dashed lines in Figure 1b: (1) total, where the whole wave fields are calculated; the heterogeneity is only present in this region; (2) reflected, where reflected wave fields are calculated; the reflected waves are defined as the reflections from the heterogeneous region (i.e., energy propagating upward), due to the incident wave; and (3) scattered, where scattered wave fields are calculated; scattered wave fields are defined as the scattering due to the presence of the heterogeneities (i.e., energy propagating leftward); for an one-dimensional model, these wave fields are zero.

Let the incident wave field be I_0, the one-dimensional solution of the wave field be T_0, the reflected wave field due to the one-dimensional model be R_0, the whole wave field be T, the reflected wave field be R and the scattered wave field be S. I, T, R, and S are either velocities (u_x, u_z) or stresses (τ_{xx}, τ_{zz}, τ_{xz}). There are general relationships among S, I, T, and R, namely,

$$T = I_0 + R; \text{ or } R = T - I_0;$$
$$S = T - T_0; \text{ or } T = S + T_0;$$
$$S = R - R_0; \text{ or } R = S + R_0.$$

The finite difference schemes are applied directly in those regions, since wave fields in those regions satisfy the wave equations individually. The explicit numerical schemes of fourth order in space and second order in time [*Levander*, 1988] are applied in the interior of those regions, whereas those of second order in space and time [*Virieux*, 1986] are used for the grid points indicated by solid symbols in Figure 1b, where special treatments are required. For example, in order to calculate the reflected shear stresses (τ_{xz}) at $n = 3$ (solid squares), the reflected horizontal velocities (u_x) at $n = 3$ (solid circles) are required. The horizontal velocities (u_x) in those positions, however, are the whole wave fields as defined above. On the other hand, in order to calculate the whole horizontal velocities (u_x) at $n = 3$ (solid circles), the whole shear stresses (τ_{xz}) at $n = 3$ (solid squares) are required. The shear stresses τ_{xz} at those positions, however, are the reflected wave fields as defined above. The whole shear stress (τ_{xz}) and reflected horizontal velocities (u_x) can be obtained by using the above three relationships among I, R, S, and T. The explicit finite difference formulations at those special regions are presented in the appendix.

2.2. Generalized Ray Theory

I_0, R_0, and T_0 can be calculated by the generalized ray theory [*Helmberger*, 1983]. With small modifications for a line source, the potentials for a receiver in a medium with a stratified velocity structure are

P wave

$$\varphi = \frac{M_0}{4\pi\rho}[\dot{D}(t) * \sum_{j=1}^{3} A_j C_j V_\alpha(t)]. \quad (1)$$

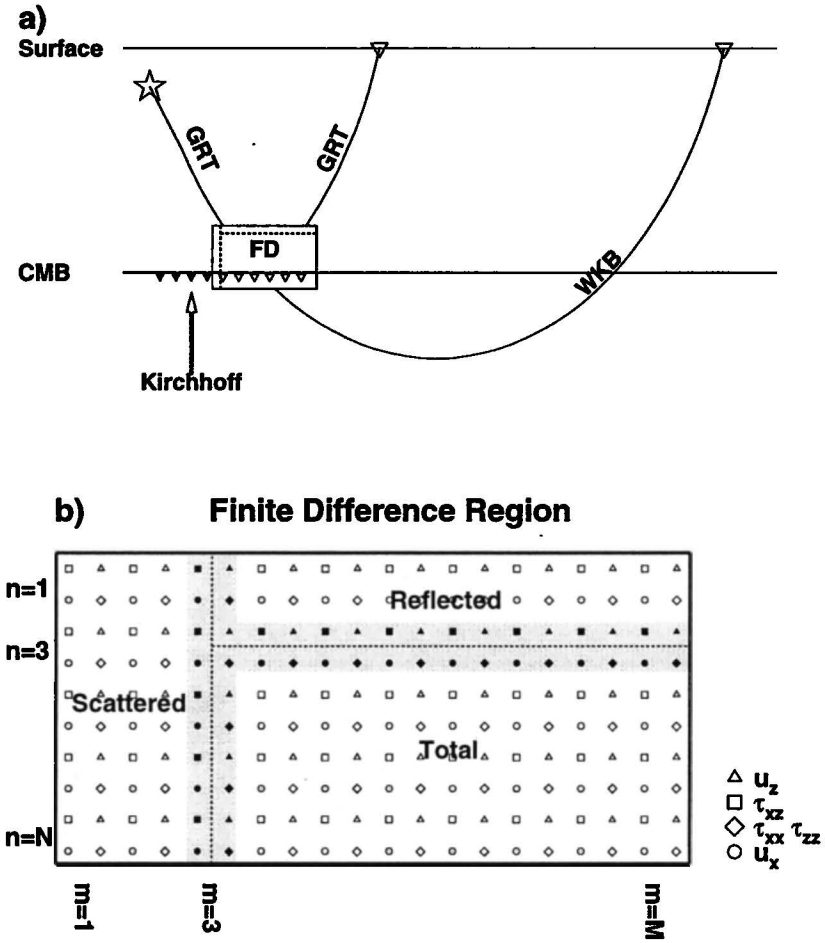

Figure 1. (a) Schematic illustration of interfacings of the hybrid method. The heterogeneous regions are assumed to be confined inside the small box, where the finite difference technique is applied. Generalized ray theory is used to calculate wave propagation from the source to the finite difference region and synthetic seismograms at the Earth's surface is obtained by integrating convolutions of the output from the source-side along the line represented by triangles and the Green's function from the receiver-side at the same positions. The source-side output in positions represented by solid triangles is calculated by the generalized ray theory; that in positions represented by empty triangles is obtained from the finite difference calculation. (b) The division of the finite difference region. The finite difference region is divided into three parts, where different wave fields are calculated (see text for detailed explanations).

SV wave

$$\Omega = \frac{M_0}{4\pi\rho}[\dot{D}(t) * \sum_{j=1}^{3} A_j SV_j V_\beta(t)], \qquad (2)$$

where

$$V_\alpha(t) = \frac{1}{\pi}[\sum_{i=1}^{n} Im(\frac{1}{\eta_\alpha}\prod(p)\frac{dp}{dt})_i],$$

$$V_\beta(t) = \frac{1}{\pi}[\sum_{i=1}^{n} Im(\frac{1}{\eta_\beta}\prod(p)\frac{dp}{dt})_i],$$

p is ray parameter, $\dot{D}(t)$ is far-field time function, $\prod(p)$ is product of the transmission and reflection coefficients, $\sum$ is summation over contributing rays, $\eta_\beta = (\beta^{-2} - p^2)^{\frac{1}{2}}$, and, $\eta_\alpha = (\alpha^{-2} - p^2)^{\frac{1}{2}}$.

The orientation constants A_j and source radiation patterns C_j, SV_j, are defined by *Helmberger* [1983]. From the relationships between stresses and displacements

$$\tau_{xx} = (\lambda + 2\mu)\frac{\partial u}{\partial x} + \lambda(\frac{\partial w}{\partial z}),$$

$$\tau_{zz} = \lambda\frac{\partial u}{\partial x} + (\lambda + 2\mu)(\frac{\partial w}{\partial z}),$$

$$\tau_{xz} = \mu(\frac{\partial u}{\partial x} + \frac{\partial w}{\partial z}),$$

where u and w are the x and z components of displacement, receiver functions for converting potentials to velocities and stresses are

For velocities

$$R_{pz} = s^2 \varepsilon \eta_\alpha,$$
$$R_{px} = s^2 p,$$

$$R_{sz} = s^3 p,$$
$$R_{sx} = s^2 \varepsilon \eta_\beta,$$

For stresses

$$R_{p\tau_{xx}} = s^2((\lambda + 2\mu)p^2 + \lambda\eta_\alpha^2),$$
$$R_{p\tau_{zz}} = s^2(\lambda p^2 + (\lambda + 2\mu)\eta_\alpha^2),$$
$$R_{p\tau_{xz}} = s^2(-2\varepsilon\mu p\eta_\alpha),$$

$$R_{s\tau_{xx}} = s^2(-2\varepsilon\mu p\eta_\beta),$$
$$R_{s\tau_{zz}} = s^2(2\varepsilon\mu p\eta_\beta),$$
$$R_{s\tau_{xz}} = s^2\mu(\eta_\beta^2 - p^2),$$

$\varepsilon = 1$ for upgoing ray and $\varepsilon = -1$ for downgoing ray.

Horizontal velocities calculated by the GRT-FD interfacing and those from GRT for an incident SV wave on the one-dimensional Preliminary Earth Reference Model (PREM) [*Dziewonski and Anderson*, 1981] show an excellent agreement in terms of both waveshape and absolute amplitude (Figure 2). The left panel shows a comparison of synthetics for receivers indicated by squares and the right panel shows a comparison of synthetics for receivers indicated by triangles. All traces are plotted to the same scale. Two primary phases are

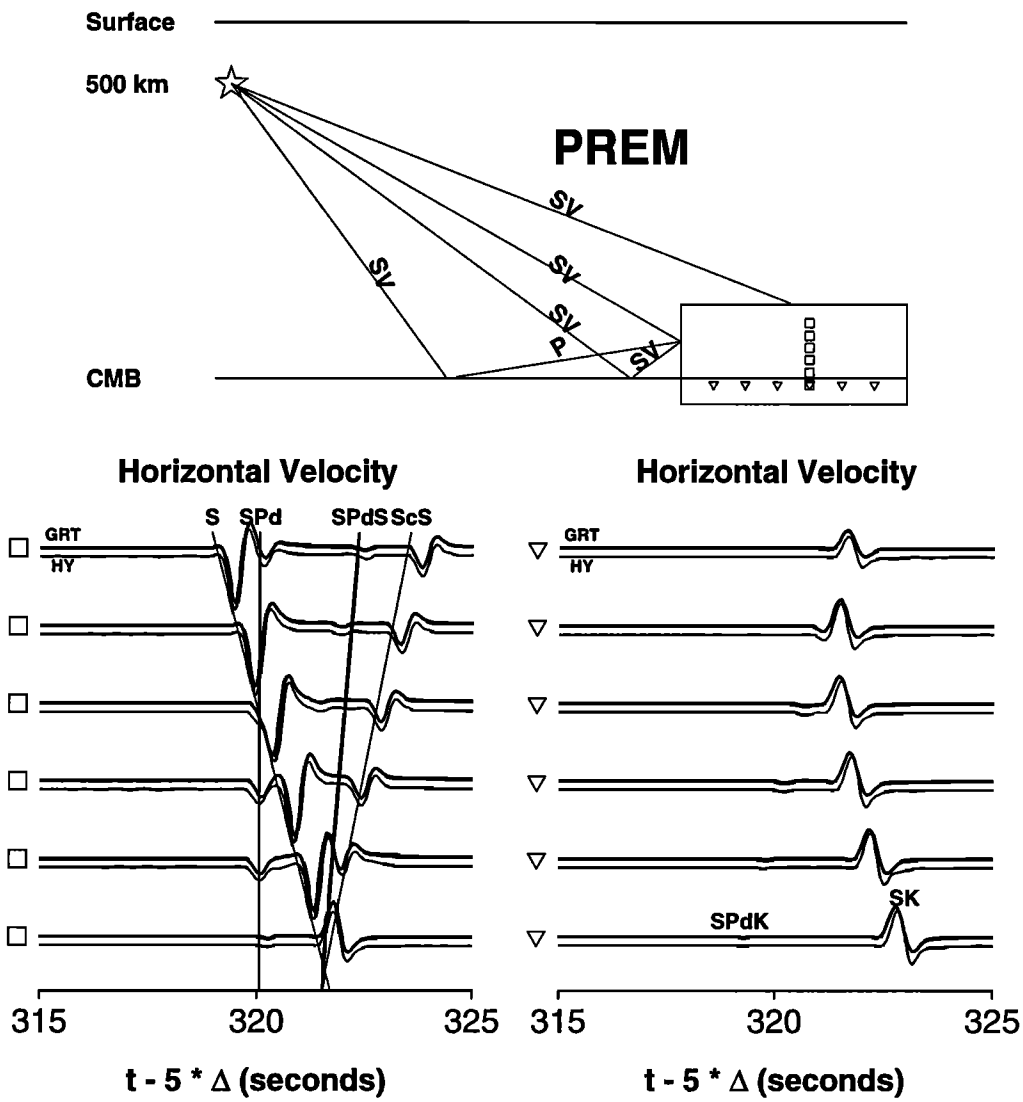

Figure 2. Comparison of horizontal velocities obtained by the generalized ray theory (heavy lines) and the hybrid method (light lines) with a source depth of 500 km. The epicentral distance of the vertical cross section is 1000 km, and the separation of vertical receivers is 8 km. The separation of horizontal receivers is 55 km. PREM is used for the calculation, and the Earth flattening approximation is applied. All seismograms are plotted to the same scale.

produced by the interaction of the incident SV wave with the core-mantle boundary, namely, an S to P reflection and an S to S reflection. The P wave from the former reflection becomes a head wave and diffracts into the core. Note that the diffracted P phase is small for PREM.

2.3. Kirchhoff Interfacing

For any two functions, u and w, there exists a relationship

$$\int_\Gamma (u\frac{\partial w}{\partial n} - w\frac{\partial u}{\partial n})dl = \iint_D (u\,\nabla^2 w - w\,\nabla^2 u)dA, \quad (3)$$

where, D is enclosed by Γ, n is outward directed normal to Γ, dl is the line integral along Γ, and dA is the areal integral in D.

The wave field potential (Q) for a seismic wave propagating in a two-dimensional whole space satisfies

$$\nabla^2 Q = \frac{1}{v^2}\frac{\partial^2 Q}{\partial t^2},$$

where v is either P or SV wave propagational velocity. The Laplace transform of the above equation over time yields

$$(\nabla^2 - \frac{s^2}{v^2})\bar{Q} = 0.$$

The Green's function ($\bar{G}$) for a line source, by definition, satisfies

$$(\nabla^2 - \frac{s^2}{v^2})\bar{G} = \delta(x-x')\delta(z-z'). \quad (4)$$

Inserting $\bar{G}$ and $\bar{Q}$ into (3), we have

$$\begin{aligned}\int_\Gamma (\bar{Q}\frac{\partial \bar{G}}{\partial n} - \bar{G}\frac{\partial \bar{Q}}{\partial n})dl &= \iint_D (\bar{Q}\,\nabla^2\bar{G} - \bar{G}\,\nabla^2\bar{Q})dA \\ &= \iint_D \bar{Q}\delta(x-x')\delta(z-z')dA,\end{aligned}$$

that is,

$$\bar{Q}(x,z) = \int_\Gamma (\bar{Q}\frac{\partial \bar{G}}{\partial n} - \bar{G}\frac{\partial \bar{Q}}{\partial n})dl. \quad (5)$$

In this study, the integration is along a straight line just below the core-mantle boundary, G is calculated by WKB technique [*Chapman*, 1976] and Q is output from the GRT-FD interfacing for regions indicated by solid triangles and directly from the generalized ray theory, for regions indicated by open triangles in Figure 1.

Since Q only applies to a P or an SV wave, it is necessary to separate the responses of P and SV waves from the output of the finite difference calculation. P and SV responses can be separated based on displacements and stresses output from the finite difference calculation

$$\vec{u} = \nabla\phi + \nabla\times\psi\vec{e}_z = \vec{u}_p + \vec{u}_s,$$

where $\vec{u}$ is displacement and ϕ and ψ are the potentials for P and SV waves respectively. Note that

$$\begin{aligned}\nabla(\nabla\cdot\vec{u}) &= \nabla(\nabla^2\phi) \\ &= \frac{1}{\alpha^2}\frac{\partial^2 \nabla\phi}{\partial t^2} \\ &= \frac{1}{\alpha^2}\frac{\partial^2 \vec{u}_p}{\partial t^2}, \quad (6)\\ \nabla\times(\nabla\times\vec{u}) &= \nabla\times(\nabla\times\nabla\times\psi\vec{e}_z) \\ &= \nabla\times(\nabla(\nabla\cdot\psi\vec{e}_z) - \nabla^2\psi\vec{e}_z) \\ &= -\nabla\times(\frac{1}{\beta^2}\frac{\partial^2\psi}{\partial t^2}\vec{e}_z) \\ &= -\frac{1}{\beta^2}\frac{\partial^2(\nabla\times\psi\vec{e}_z)}{\partial t^2} \\ &= -\frac{1}{\beta^2}\frac{\partial^2 \vec{u}_s}{\partial t^2}. \quad (7)\end{aligned}$$

Thus, Q in (5) can take the forms of $\nabla(\nabla\cdot\vec{u})$ and $\nabla\times(\nabla\times\vec{u})$, which are equivalent to accelerations caused by P and SV waves, respectively. $\nabla(\nabla\cdot\vec{u})$ and $\nabla\times(\nabla\times\vec{u})$ can be obtained from the displacements and stresses output from the finite difference calculation.

$$\begin{aligned}\nabla(\nabla\cdot\vec{u}) &= \nabla(\tfrac{\partial u_x}{\partial x} + \tfrac{\partial u_z}{\partial z}) \\ &= \nabla(\tfrac{\tau_{xx}+\tau_{zz}}{2(\lambda+\mu)}) \\ &= \tfrac{\partial}{\partial x}(\tfrac{\tau_{xx}+\tau_{zz}}{2(\lambda+\mu)})\vec{e}_x + \tfrac{\partial}{\partial z}(\tfrac{\tau_{xx}+\tau_{zz}}{2(\lambda+\mu)})\vec{e}_z, \\ \nabla\times(\nabla\times\vec{u}) &= \tfrac{\partial}{\partial z}(\tfrac{\partial u_x}{\partial x} - \tfrac{\partial u_z}{\partial z})\vec{e}_x + \tfrac{\partial}{\partial x}(\tfrac{\partial u_z}{\partial z} - \tfrac{\partial u_x}{\partial x})\vec{e}_z.\end{aligned}$$

$\nabla(\nabla\cdot\vec{u})$ and its z derivative calculated by GRT and those obtained by the FD-GRT interfacing show an excellent agreement (Figure 3). Again, all traces are plotted to the same scale and PREM is assumed.

The point source solution can be obtained by correcting the line source response [e.g., *Stead and Helmberger*, 1988]:

$$U_{point} = \frac{2}{\sqrt{R}+\sqrt{x}}\frac{1}{\sqrt{t}} * \frac{d}{dt}U_{line}, \quad (8)$$

where R and x are the total and horizontal distances, respectively.

For Earth models similar to PREM, SV wave reaches a critical angle at the core-mantle boundary and bifurcates into an *SKS* and a diffracted P (*SPdKS*) propagating along the boundary at a distance of about 106° [*Choy*, 1977] (Figure 4). Synthetics waveforms obtained from the GRT-FD-Kirchhoff interfacing and those by the generalized ray theory show reasonable agreement except the difference in the frequency content of the *SPdKS* phase at large distances (Figure 4). The discrepancy is caused by the lack of long-period diffracted energy obtained from the WKB synthetics [*Chapman and Orcutt*, 1985; *Helmberger et al.*, 1996]. The difference becomes less noticeable when *SPdKS* contributions dominate the synthetics for models with ultra-low-velocity zones.

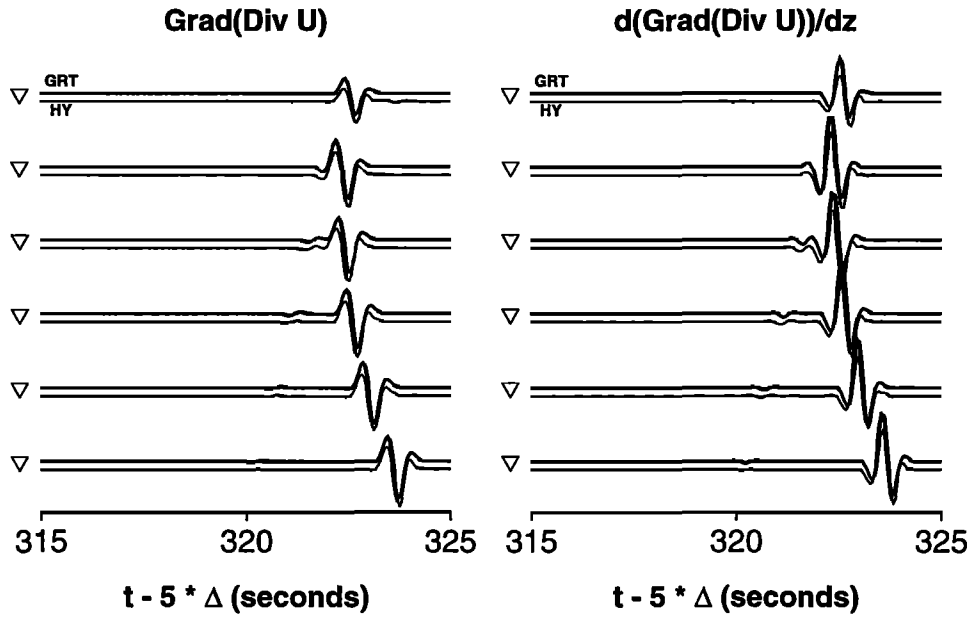

Figure 3. Comparison of quantities $\nabla(\nabla \cdot U)_x$ and, $d(\nabla(\nabla \cdot U)_x)/dz$ obtained by the generalized ray theory (light traces) and the hybrid method (heavy traces). All synthetics are plotted to the same scale. The receivers are indicated in Figure 2.

3. Application to Modeling *SKS-SPdKS* Phases Through Ultralow Velocity Zones

SKS-SPdKS waveforms are very sensitive to the localized structures near the core-mantle boundary and provide ideal localized samplings of these structures. In the meantime, the almost identical ray paths of *SKS* and *SPdKS* in the mantle (Figure 4) and the nearly homogeneous outer core structure minimize the uncertainties of waveform modeling due to crust and mantle heterogeneities and seismic source radiation pattern.

Figure 5 displays a sample of anomalous *SKS-SPdKS* waveforms, recorded at long-period World-wide Standard Seismic Network (WWSSN) stations in North America, for two Fiji and one Kermadec events. The large relative time lags of *SPdKS* phases with respect to *SKS* and the small critical distance for *SKS* are obvious in the data, as opposed to the predictions (dashed lines) from PREM (Figure 5). The arrival times in the average data can be fit by a model with a 10% drop of *P* velocity at the mantle's base (dotted line) [*Garnero and Helmberger*, 1996]. Contrary to those predicted by PREM, the diffracted *SPdKS* phases at some distances (e.g., 110°) become strong geometrical arrivals if a low-velocity layer is present just above the core-mantle boundary [*Helmberger et al.*, 1996]. The considerable variation of observed waveforms has been modeled in terms of ultralow-velocity layers at the bottom of mantle with variable layer thicknesses ranging from 5 to 40 km, drops in *P* and *S* velocities of 10%, and the density of PREM [*Garnero and Helmberger*, 1996]. If the low-velocity layer, however, is caused by partial melting, an *S* velocity drop of about 30% will be expected for a *P* velocity drop of 10% [*Williams and Garnero*, 1996]. In that case, the converted *S* to *P* phase at the upper boundary of ultralow-velocity layers becomes discernible in synthetics, unlike the data. Unless the thickness of the layer is less than about 10 km, the separation in timing between the *SKS* and the converted phases is small and not observable at long-period waveforms [*Garnero and Helmberger*, 1998]. Models with flat layers encounter a further conceptual problem when the waveform variation continues down to small scales, as documented by *Garnero and Helmberger* [1998]. Essentially, to match the waveforms requires that the variation in layer thickness approaches the lateral sampling separation, in violation of Huygen's principle. Moreover, some very anomalous records, such as those labeled by the dots in Figure 5, remain unexplained with current modeling techniques. Given these modeling difficulties and large velocity variations, it appears particularly important and necessary to investigate the effects of nonplanar structures by numerical methods, as strongly suggested by the rapid variations of the observed waveforms. In this section, we perform *SKS-SPdKS* waveform sensitivity studies for various two-dimensional structures in the first part and model the Fiji data in the second part.

3.1. Sensitivity Studies

In this section, we explore the waveform complexity produced by various two-dimensional structures. To reduce the parameter space, we consider mostly sim-

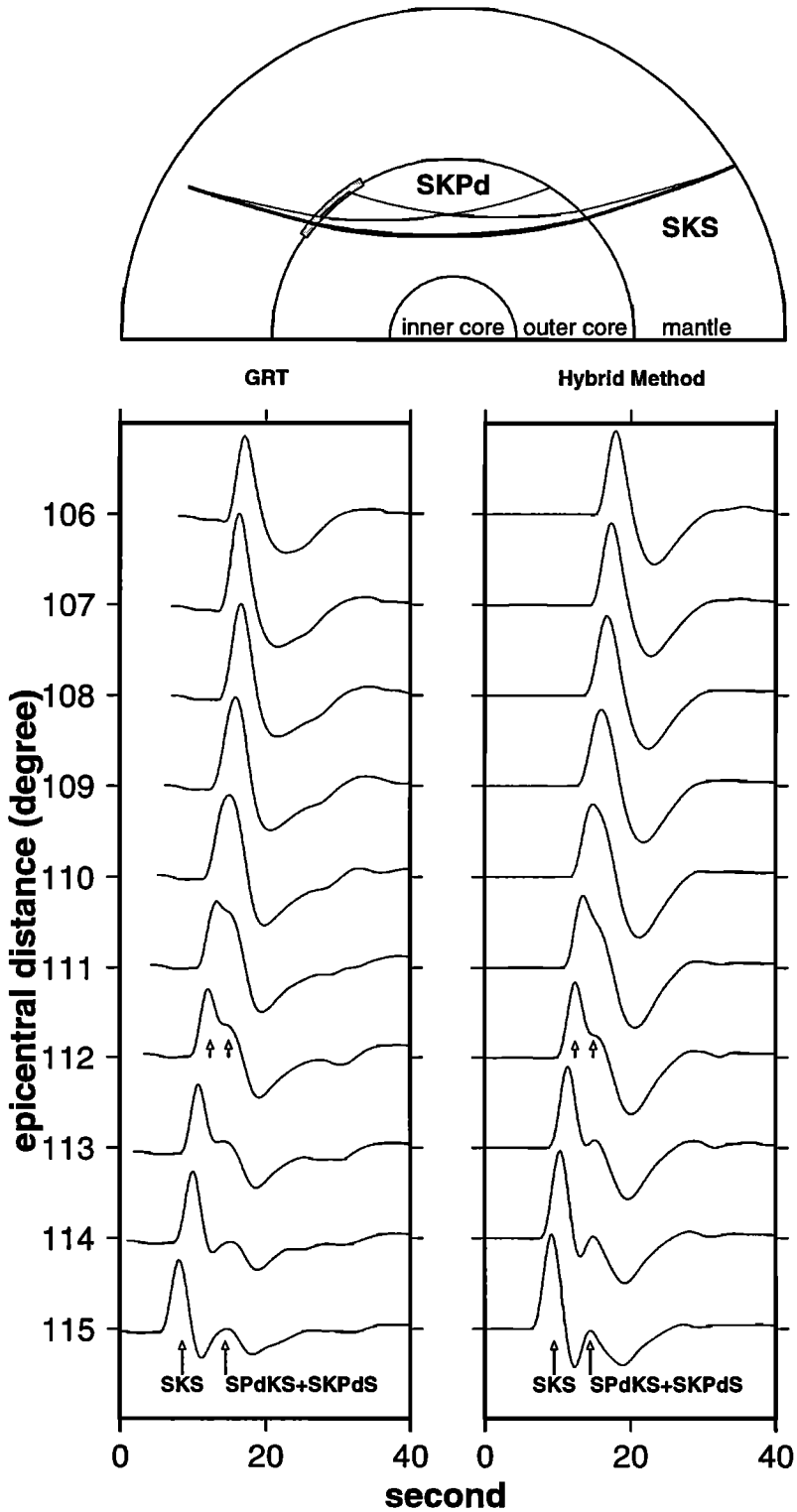

Figure 4. Ray paths of *SKS-SPdKS* phases and comparison of *SKS-SPdKS* synthetics obtained by the generalized ray theory and the hybrid method. Synthetics have been convolved with the long period instrument response of the World-Wide Standard Seismic Network (WWSSN) with $t^* = 1$ and a trapezoidal source time function (1,1,1). All traces are self normalized. PREM and a source depth of 500 km are used for the calculation. The shaded area is the finite difference region.

ple dome-shaped structures just above the core-mantle boundary. These structures produce waveforms best fit to the data. In most cases, we adopt an 1 to 3 ratio of P and S velocity drops of the seismic anomalies, which is favored on the physical ground of partial melt [*Williams and Garnero*, 1996], although other values of this ratio are also considered. We examine effects of various dimensions (in height and width), seismic parameters, and position.

We begin by exploring effects of dome curvature for an impinging SV wave. The dome is assumed to have a P velocity reduction of 10%, an S velocity reduction of 30% and a density increase of 20%, with respect to PREM. These parameters are obtained by assuming a partial melting origin [*Williams and Garnero*, 1996]. PREM is used elsewhere. The dome starts just before the SV wave reaches the critical angle at about 770 km and ends at 1043 km (Figure 6a). Figure 6b shows the important phases for generating the *SPdKS-SKPdS* phase at the surface of the Earth. *SKPdS* is formed as an *SSK* wave on the source side and a *KPdS* wave on the receiver side of the mantle and *SPdKS* is formed as an *SPdK* and an *SPK* on the source side and a *KS* on the receiver side of the mantle. Snapshots of wave propagation are shown in Figures 6c-6f. At $t = 384.25$ s, only the incident SV wave is present (Figure 6c). The converted and reflected phases due to the dome structure at later times are labeled in

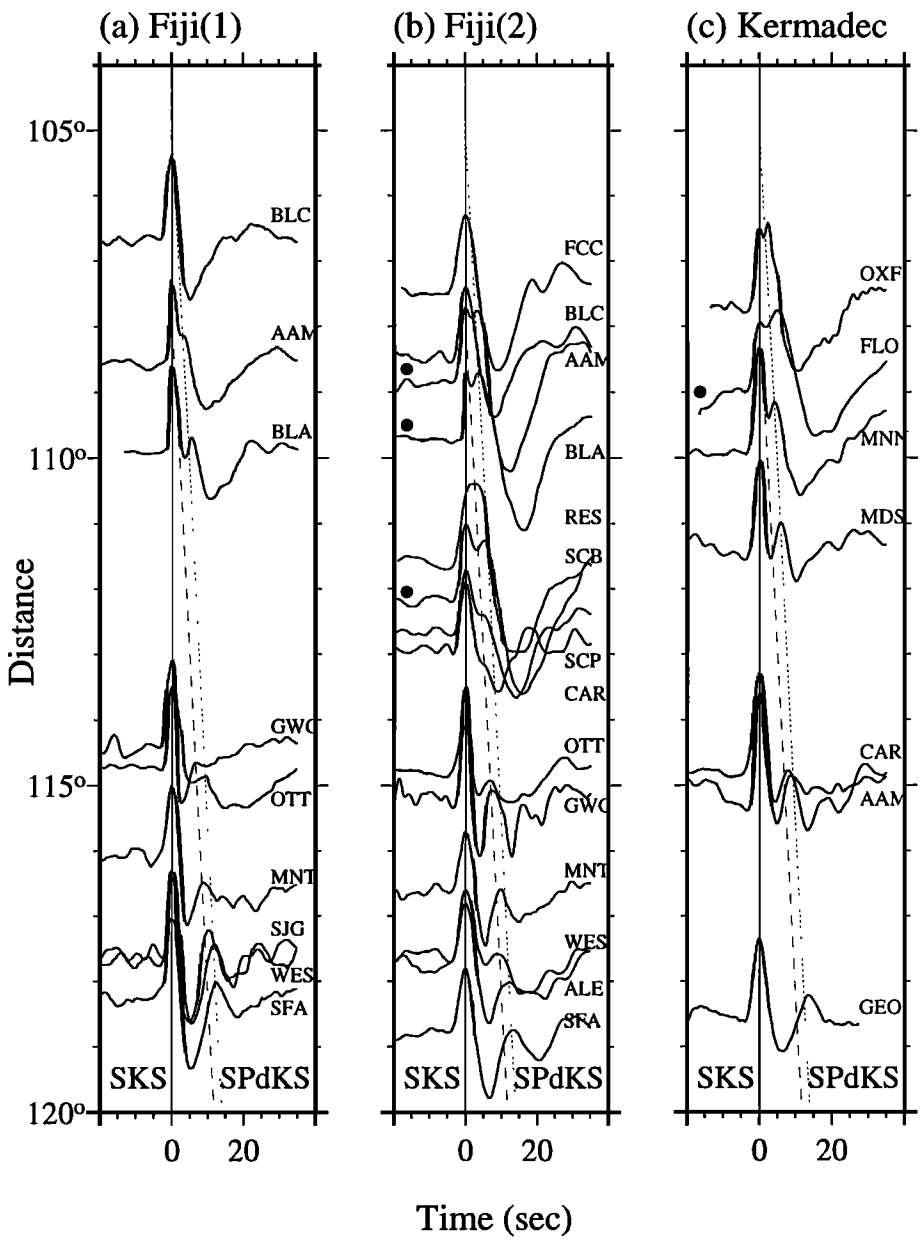

Figure 5. Observed *SKS-SPdKS* seismograms for two Fiji and one Kermadec events and predicted arrivals of *SKS* and *SPdKS* phases for PREM (dashed lines) and a model with a P velocity drop of 10% at the mantle's base (solid lines).

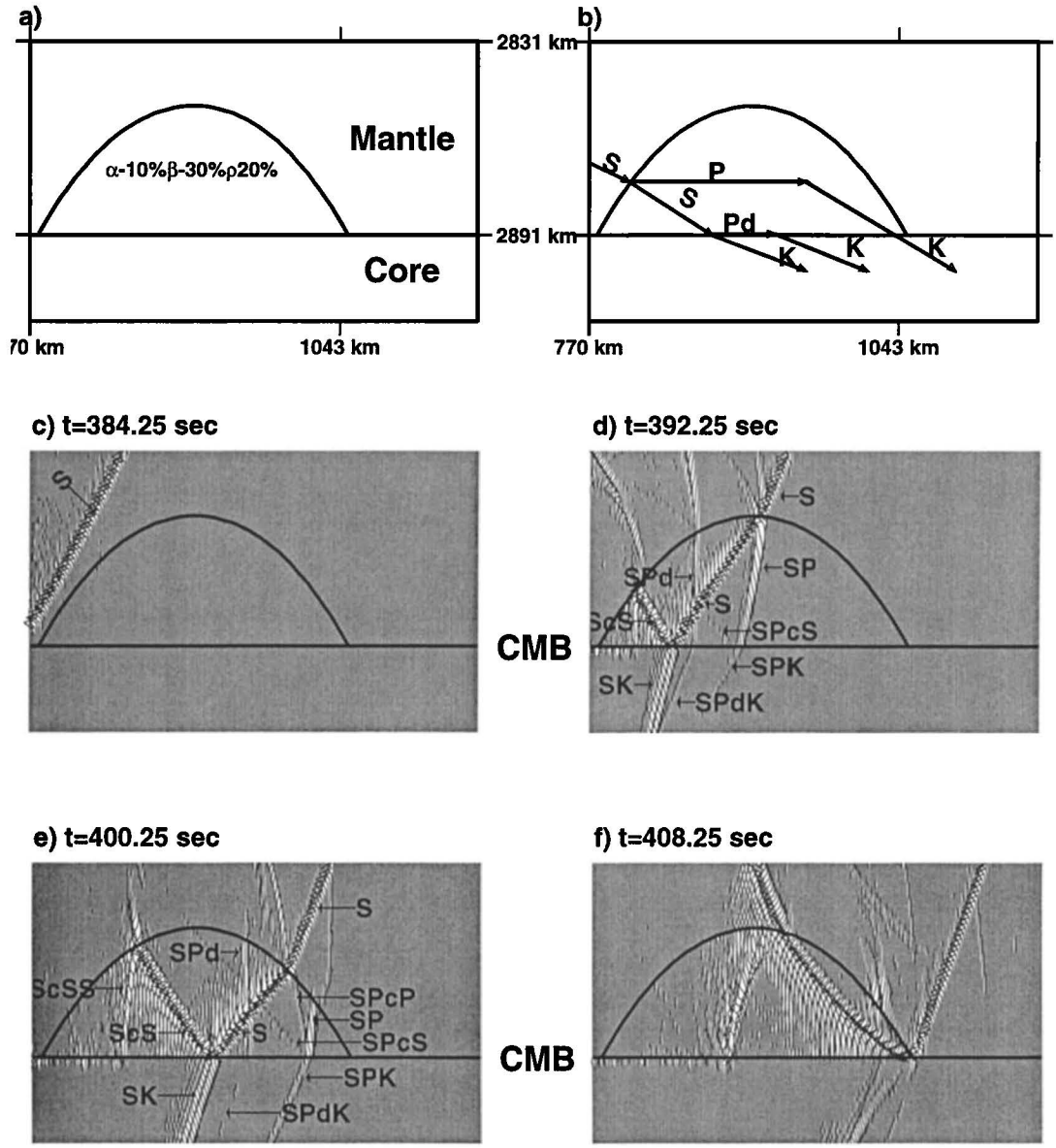

Figure 6. Wave propagation for a model with a dome-like structure just above the core-mantle boundary. PREM is used and the dome has a P velocity reduction of 10%, an S velocity reduction of 30%, and a density increase of 20% with respect to PREM. These parameters are obtained by assuming partial melt with a P velocity drop of 10%. (a) Model setup; (b) important phases for generating *SKS-SPdKS* waves at the surface of the Earth; (c)-(f), snapshots of the wave fields.

Figures 6d-6f. *SPdK* is relatively small because it is a diffracted arrival, while the *SPK* phase is strong because it is locally a geometrical arrival (e.g., Figure 6e).

The propagational effects of ultralow-velocity zones are demonstrated by the *SKS-SPdKS* total waveforms and contributions from different segments of the core-mantle boundary, separated by the Kirchhoff integral on the source side (Figure 7). The division of segments is shown in the top panel. The PREM synthetics are also shown in dashed lines for comparison. Contributions from the segment 1 are exactly matched for both models, since the wave propagation is not affected by the presence of the ultralow-velocity zone. For the contributions from the segment 3, waveforms predicted by the dome structure are in good agreement with those of PREM, except that they are delayed by the ultralow-velocity zone. For the *SKS-SPdKS* wave groups contributed by the segments 2 and 1, in addition to the delays of waveforms caused by the ultralow-velocity zone, the reduced amplitudes of these *SKS-SPdKS* phases produced by the model with the ultralow-velocity zone are also obvious. The delays break down the coherence of *SKS* at small distances (106°-110°) and partition the *SKS* energy into two phases. Note that the maximal amplitudes of synthetics predicted by the dome structure are smaller than

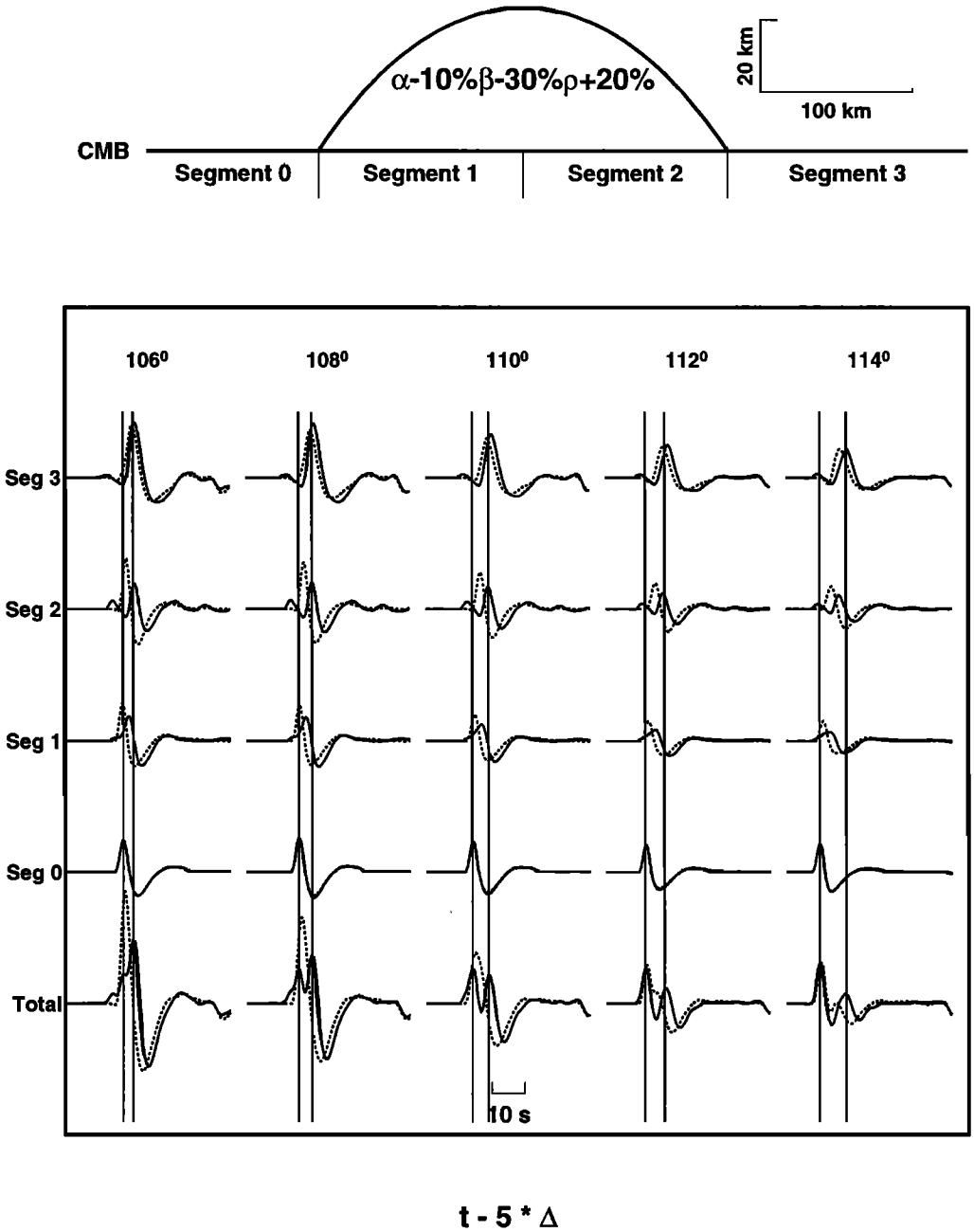

Figure 7. The total *SKS-SPdKS* waveform synthetics along with contributions to *SKS-SPdKS* synthetics from different segments of the core-mantle boundary on the source side. The dashed traces are those for PREM, and heavy traces are calculated with the dome structure shown in Figure 6. The source depth is 500 km.

those of PREM at these distances, because some energy of the incident *SV* wave is reflected back into the mantle due to the curved structure and some *SKS* energy is partitioned into *SPdKS* and *SPKS* phases. The latter phase has a path similar to *SKS* except that it propagates as a converted *P* wave in the ultralow-velocity zone. *SPKS* appears as a precursor in the contributions from the segment 2. Those precursors will become more obvious if the dome structure is under the entry point of *SKS* phase. At larger distances, the dome structure affects mostly the *SPdKS* phases, since the dome structure is far away from the entry point of *SKS* at these distances. It is also obvious from snapshots that the dome structure will produce strong precursors to *ScP* and *ScS*.

Figure 8 shows snapshots of wave propagation for a boxcar structure for the same model setup in Figure 6. Although broadband *SKS-SPdKS* synthetics for the model with a dome-shaped structure and that with a boxcar structure are distinguishable, the long-period

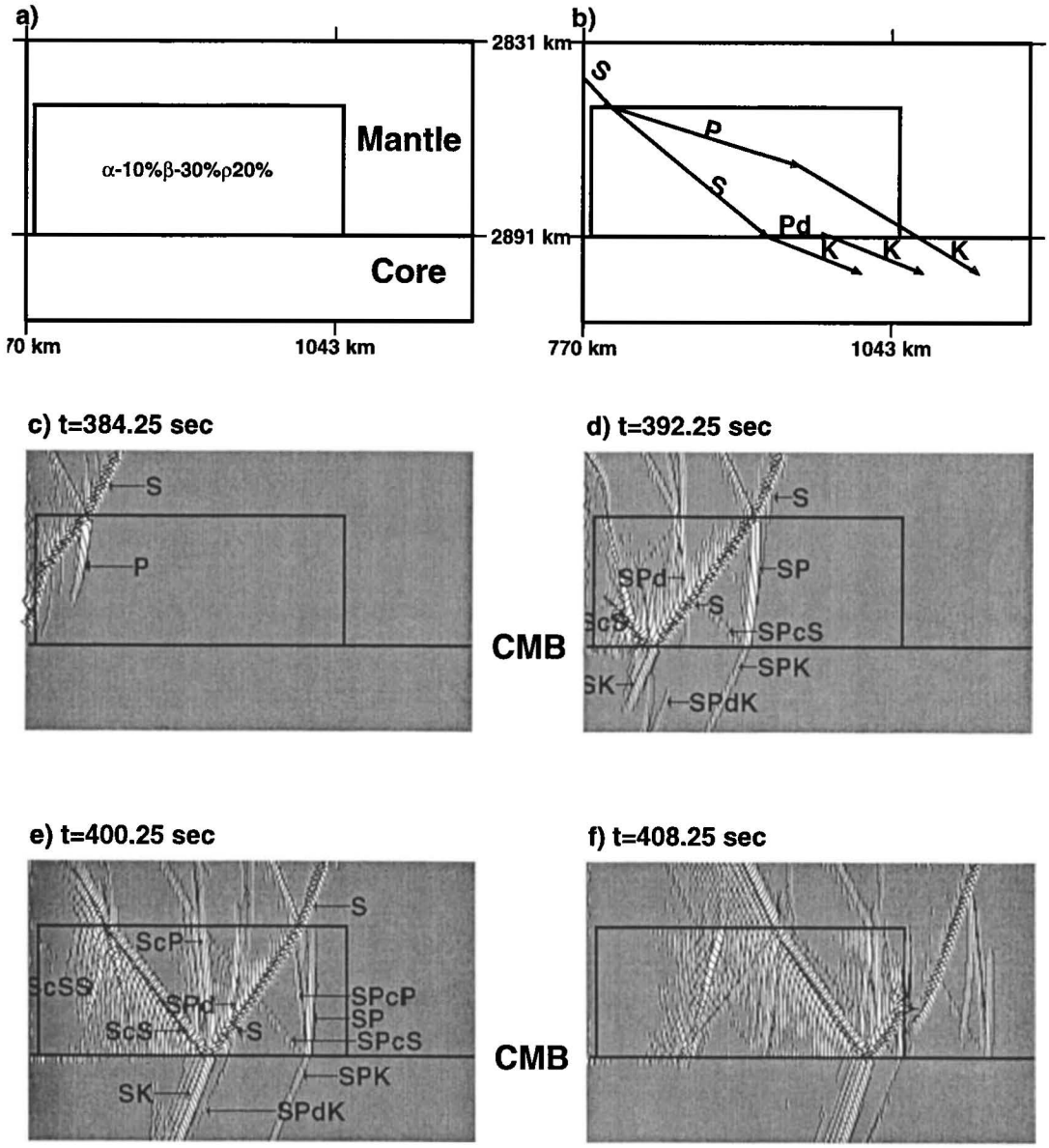

Figure 8. Same as Figure 6, except that the low-velocity region is a boxcar.

WWSSN synthetics, however, are very similar for these two structures with these dimensions (Figure 9). For the boxcar structure, precursors to *SKS* are stronger because of a stronger *S* to *P* conversion from the mantle to the structure, compared to the case of the dome-like structure (Figure 6). If the boxcar structure extends to larger distances, synthetics will become even more complex, with many converted phases even for long-period synthetics, similar to the predictions from one-dimensional models with ultralow-velocity layers.

Since the multiples are strongly influenced by the geometrical location of the *S* to *P* critical angle, the location of two-dimensional structures becomes a controlling factor in modeling *SKS-SPdKS* waveforms, as demonstrated in the synthetic record sections for dome-like structures located in various positions above the core-mantle boundary (Figure 10). The synthetics are convolved with a trapezoidal (1,1,1) source time function and the long-period WWSSN instrument response. The *SV* critical points (heavy arrows) and the *SKS* entry points for epicentral distances 105° and 115° at the core-mantle boundary are shown in Figure 10. In Figure 10a, the dome structure is in the position that affects *SKS* phase very little for epicentral distances less than 105°; small precursors are present for the distance ranges 103°-109° and the dome structure distorts *SKS* severely for distance ranges 111°-115°. Synthetics in Figure 10b show the same characteristics as those in Figure 10a, except that the separation between *SKS* and *SPKS* becomes more obvious at distance ranges 111°-115°. Note the complex waveforms at those distances in Figure 10b. In Figure 10c, the dome structure has little

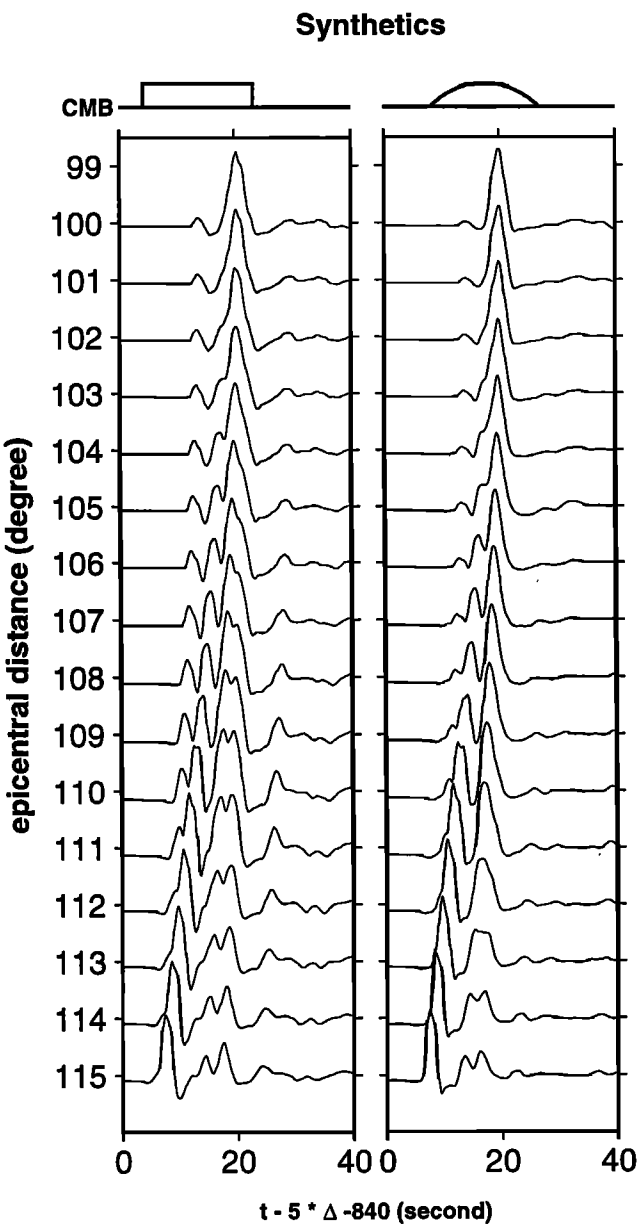

Figure 9. The broadband synthetic *SKS-SPdKS* waveforms for models shown in Figures 6 and 8. The synthetics are obtained by convolving the Green's functions with a source time trapezoidal function (1,1,1) and $t^* = 1$.

effect on the *SKS* phase at distances greater than 114°, since anomalies are no longer beneath the entry points of *SKS* at those distances. The dome structure becomes important in affecting the timing and waveshape of *SKS-SPdKS* phases, as is obvious in the synthetics at distance ranges 108°-113°. The second phase appears even stronger than the first one at some distances (e.g., 109°). Waveform distortions appear at smaller distances in the synthetics shown in Figures 10d-10e.

Long-period *SKS-SPdKS* synthetics are also sensitive to the dimensions (height and width) and seismic parameters of the dome-shaped structures, although some trade-offs exist among these parameters (Figure 11). The synthetics in Figure 11a are calculated with a 40-km-high and 136-km-wide dome-shaped structure, located 136 km beyond the *SV* critical point. Synthetics produced with this dome-shaped structure, though different from those produced by PREM, are near the threshold of detectability of difference. Synthetics in Figures 11b-11c are obtained for models of 40-km-high domes with horizontal length scales of 267 and 534 km. The domes are now located just after the critical distance for *SV* waves. Note the significant difference between synthetics in these two panels. The *SPdKS* phases are very small for the model with a 534 km dome because the dome structure attenuates *SPdKS-SKS* phases over a longer distance. The second phase and the *SPdKS* phase become very weak compared to the first *SKS* phase. Synthetics for an 80-km-high dome with a width of 136 km are shown in Figure 11d. The *SPdKS* phases appear stronger than the *SKS* phase in this case, and this structure produces strong precursors to the *SKS* phase, especially at distance ranges 109°-112°. The Figure 11e shows synthetics for the same dome with different velocity reductions. A substantial trade-off exists between velocity reduction and the vertical dimension of dome structures. While a higher dome tends to increase the strength of the *P* diffraction, delay its arrival time and thus make it a more recognizable phase, a lower *S* velocity, on the other hand, tends to move the critical angle to a closer distance, reduce the strength of *SKS* and thus produce a similar waveform. Note that the synthetics from the 40-km dome with a drop of 20% in *S* velocity (Figure 11b) look similar to those of an 80-km dome with a drop of 10% in *S* velocity (Figure 11e). For the larger dome, however, precursors appear in *SKS-SPdKS* synthetics at distance ranges 109°-113°, and stronger *SPdKS* arrivals exist at larger distance ranges.

Long-period *SKS-SPdKS* waveforms are not very sensitive to the smoothness and roughness of those seismic structures, since these long-period waveforms are the average effects of the structure (Figure 12). Long-period synthetics for a dome with multilayers (Figures 12a and 12c) are similar to those of models with a single dome and long-period synthetics from an extremely rough curvature (Figures 12b and 12d) are similar to those with smooth structures.

3.2. Ultralow-Velocity Zones Beneath the Southwest Pacific

The above sensitivity studies have demonstrated a variety of *SKS-SPdKS* waveform complexities required for matching anomalous observed waveshapes not explainable with flat-layer models. A unique interpretation of this two-dimensional modeling of the data becomes more problematic because of the trade-offs among parameters. From example, the trade-off be-

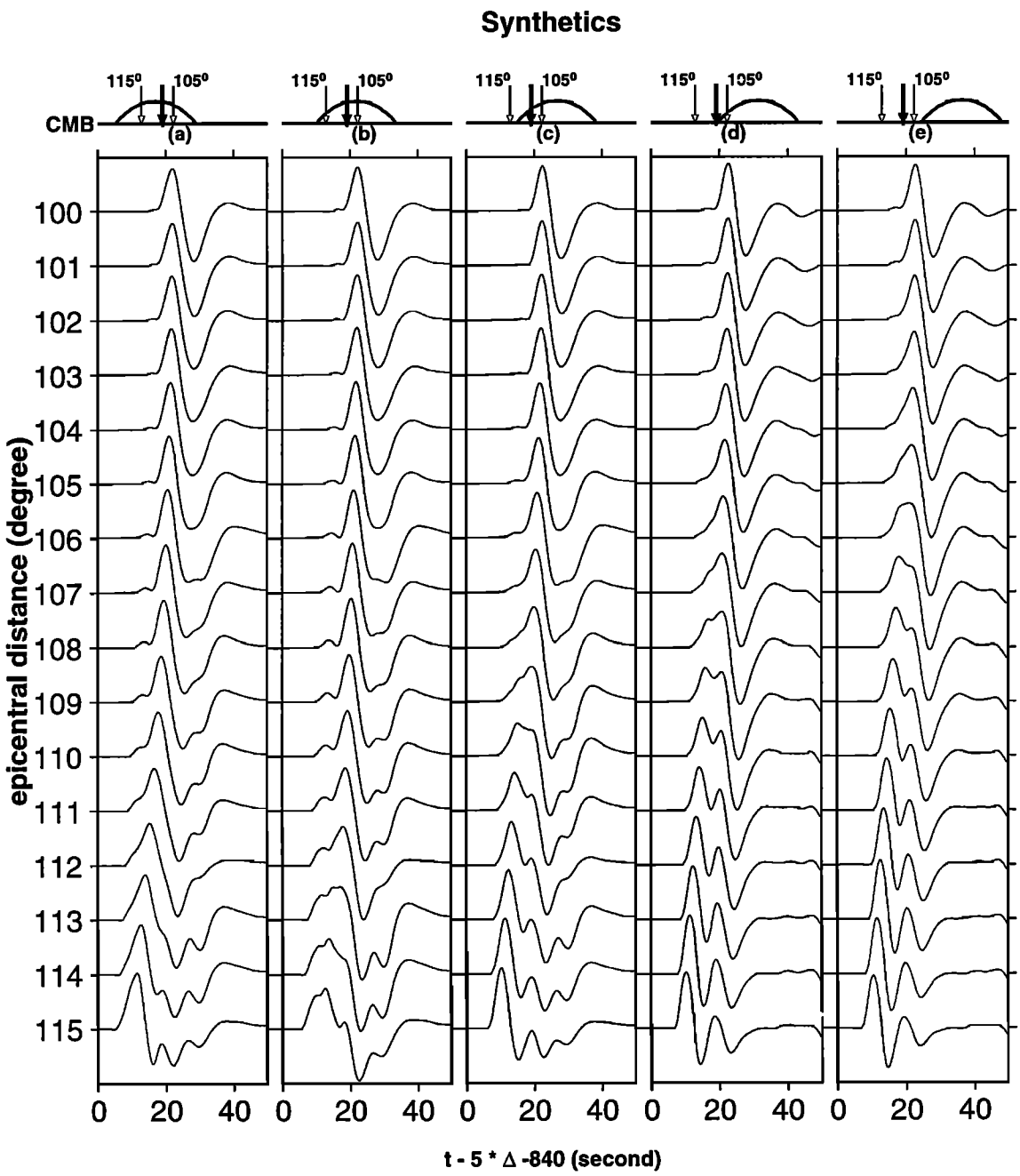

Figure 10. Synthetic *SKS-SPdKS* waveforms for models with dome-like structures just above the core-mantle boundary on the source side. Domes have a horizontal scale of 267 km, a thickness of 40 km, a P velocity reduction of 10%, an S velocity reduction of 30%, and a density increase of 20% with respect to PREM. Different panels of synthetics correspond to different positions of the dome-like structures. The entry points of *SKS* phase for distance ranges at 105° and 115° are shown, and the critical distances for *SKS* at the core-mantle boundary are indicated by heavy arrows. All synthetics have been convolved with the long-period WWSSN instrument response with $t^* = 1$ and with a source time trapezoidal function (2,2,2). The source depth is 500 km and PREM is assumed elsewhere.

tween the density change and geometry of the structure makes the density change unresolvable. Nevertheless, useful information about these localized structures, such as the P velocity reduction, general dimensions, and S velocity drops required, can be extracted from the data. For example, a P velocity drop of 10% is required to fit the travel times of the *SPdKS* phases, localized structures with horizontal length scales of at least 100 km are required to produce anomalous long-period *SKS-SPdKS* waveform, localized structures with

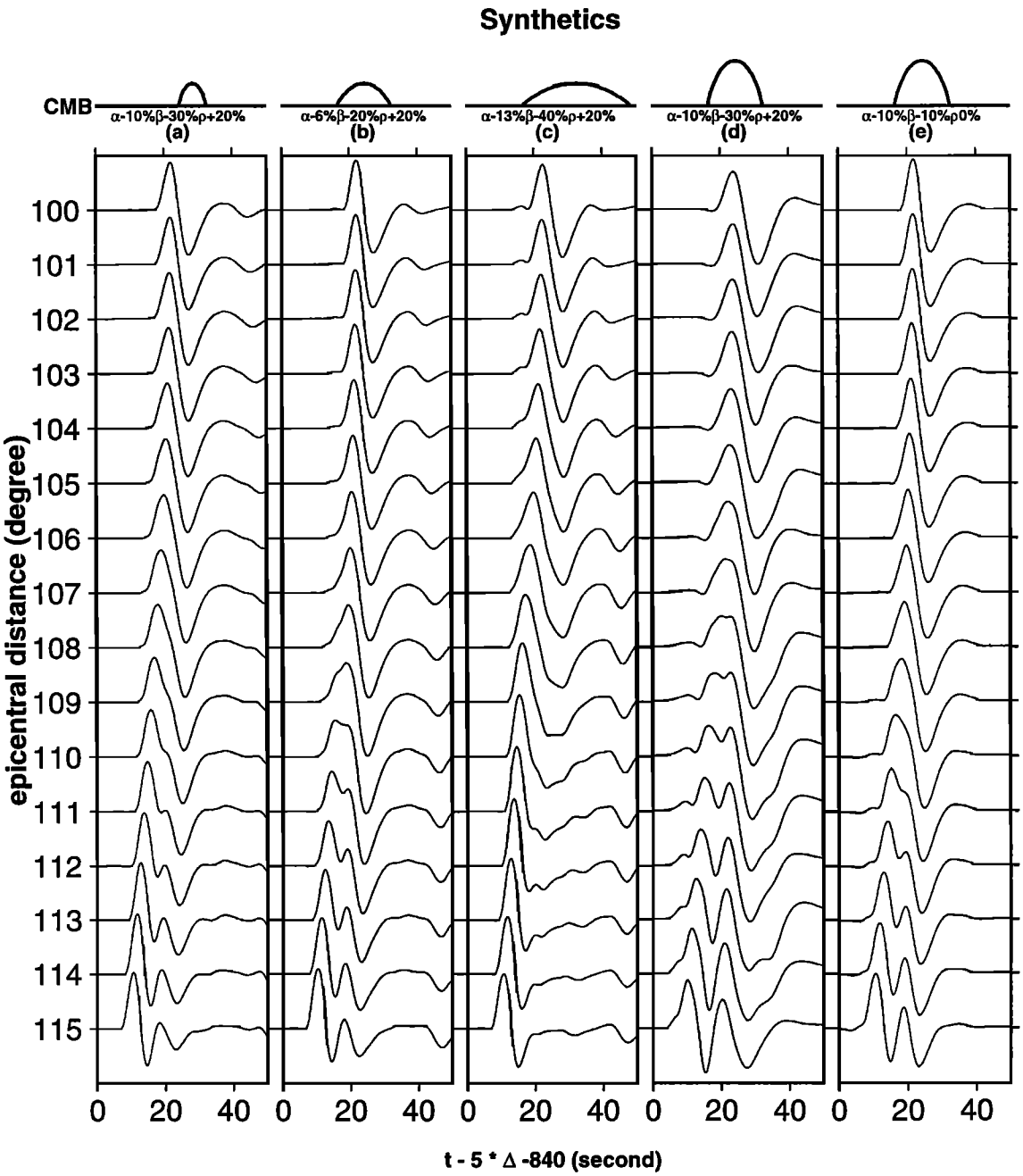

Figure 11. Synthetic *SKS-SPdKS* waveforms for models with different dome structures just above the core-mantle boundary. All synthetics have been convolved with the long-period WWSSN instrument response with $t^* = 1$ and with a source time trapezoidal function (2,2,2). The source depth is 500 km and PREM is assumed elsewhere. The horizontal length scales for models from Figures 11b-11e are 267 km, whereas that for model in Figure 11a is 133.5 km. The heights of the dome are 40 km in Figures 11a-11c and 80 km in Figures 11d and 11e.

vertical length scales of more than 80 km will generate noticeable precursors to *SKS* phase, and an *S* velocity drop of 30% rather than 10% is favored, etc.

The observed *SKS-SPdKS* waveforms shown in Figure 5 can be explained by a simple dome-like structure just above the core-mantle boundary. For example, the observed waveforms for the Fiji 1 event can be explained by the synthetics shown in Figure 10e; the observed waveforms for the Fiji 2 event can be explained by the synthetics shown in Figures 10b and 10c; and the observed waveforms for the Kermadec event can be explained by the synthetics shown in Figures 10d and 10e. Figure 13 shows some comparisons of some of the most anomalous observations with these synthetics. Only observations along the most similar azimuth are chosen (see Figure 13 (top) for geometry). The corre-

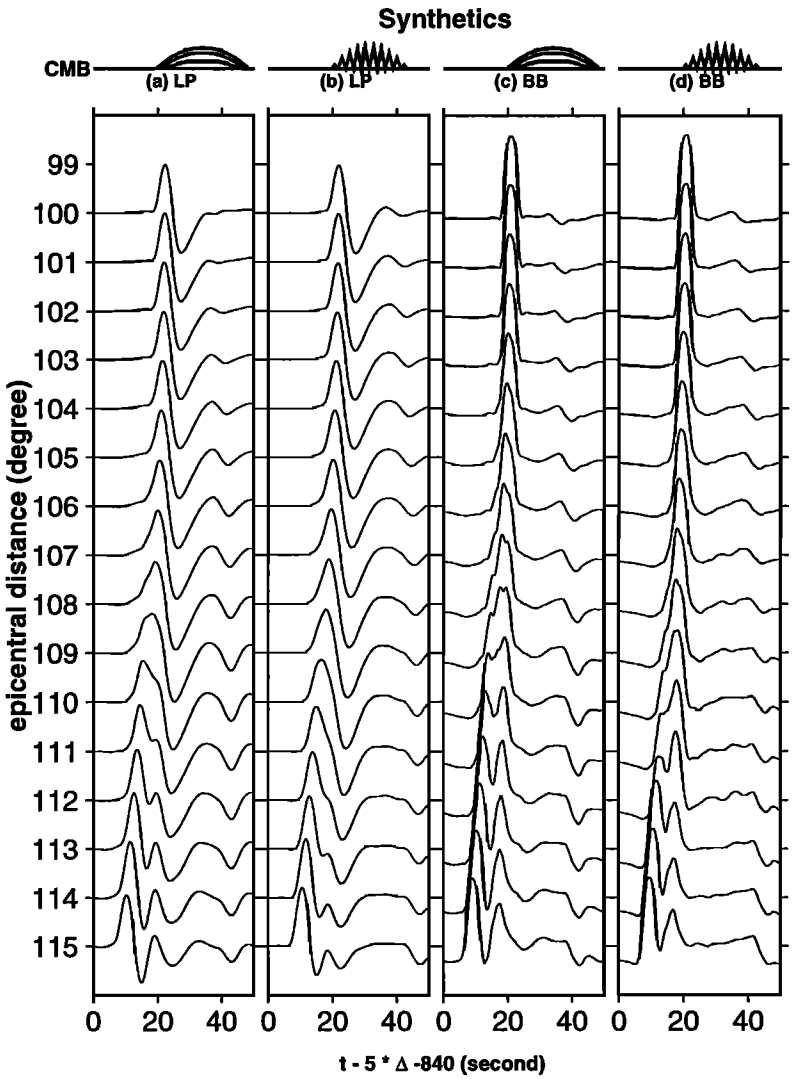

Figure 12. Long-period (LP) and broadband (BB) synthetics for models with different dome structures just above the core-mantle boundary. Synthetics in Figures 12c and Figures 12d have been convolved with $t^* = 1$ and with a source time trapezoidal function (2,2,2). Synthetics in Figures 12a and 12b have also been convolved with the long-period WWSSN instrument response. The source depth is 500 km and PREM is assumed elsewhere. The model used in Figures 12a and 12c consists of three layers with P velocity reductions of 3%, 6% and 10%, SV velocity reductions of 10%, 20% and 30%, and density increases of 7%, 14% and 20% from outer to the inner layers. The models used in Figures 12b and 12d have roughness and a P velocity reduction of 10%, an SV velocity reduction of 30%, and a density increase of 20%. All structures have horizontal length scales of 250 km. Note that *SKS-SPdKS* synthetics are not sensitive to the smoothness of the transition to the localized structures and the roughness of those seismic structures.

sponding synthetics are selected from Figure 10, where the only variable is the position relative to the critical angle. The observed waveforms at BLC and AAM can simply be explained by shifting the dome position by 100 km. The observation of SCB and SCP has been fit by just averaging Figures 10b and 10c as a rough approximation of a smaller shift interval. Our best simplified picture of the ultralow-velocity zones based on this fit is given in Figure 13 (middle).

It should be emphasized again that because of the nature of long-period data, the structure shown in Figure 13 should be considered a tentative picture. Some of the uniqueness problems can be addressed by broadband data and information from other phases, such as *SKKS, PKP, PcP, ScP* and *ScS*, etc. For example, the amplitude ratio of *SKKS/SKS* can be useful in distinguishing the synthetics of a 40-km-high dome with a 20% drop in S velocity from those of an 80-km-high dome with a 10% drop in S velocity. The roughness and smoothness can also be constrained by short-period or broadband data, as demonstrated in the studies of short-period and broadband scattered precur-

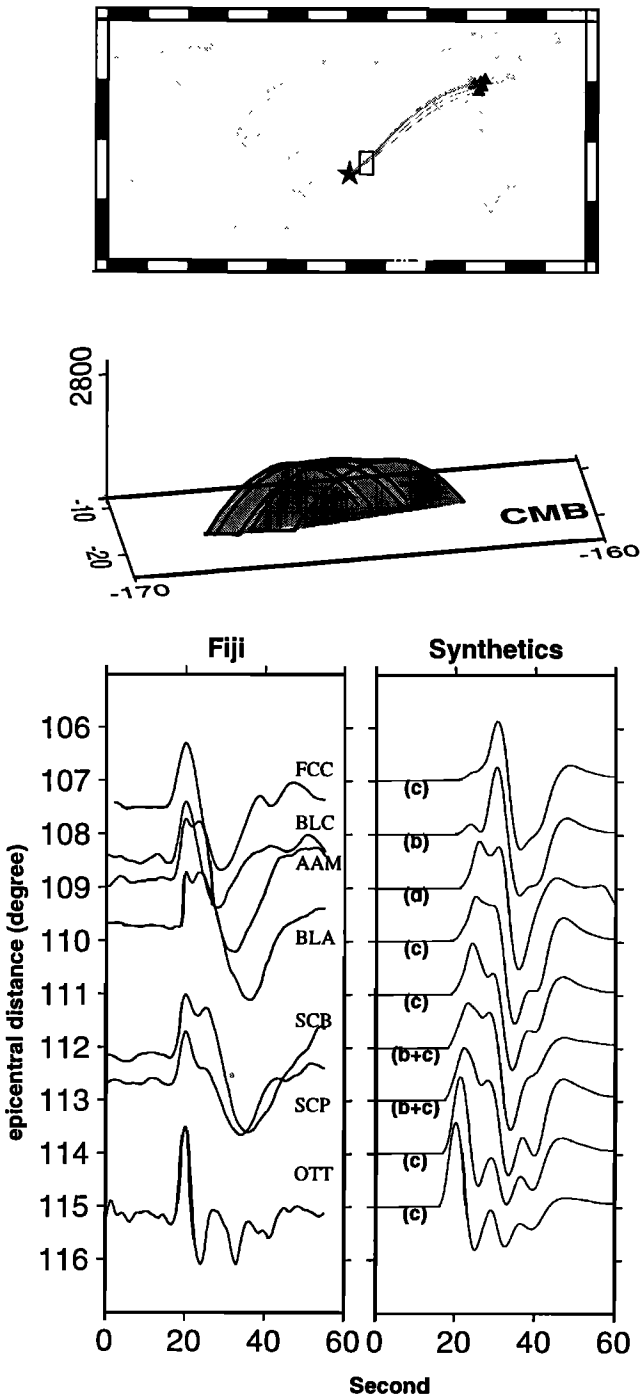

Figure 13. The comparison of synthetics and observed waveforms for a Fiji event and the geometry of a three-dimensional structure for producing the synthetics. The seismic anomaly has a P velocity drop of 10%, an S velocity drop of 30%, and a density increase of 20% with respect to PREM. Synthetics are chosen from Figure 10 and labeled.

sors to *PKP* [*Vidale and Hedlin*, 1998; *Wen and Helmberger*, 1998]. Three-dimensional effects of the seismic structures are also potentially important.

4. Conclusion

A two-dimensional *P-SV* hybrid method is developed, which combines generalized ray theory, finite difference, WKB and the Kirchhoff theory. The generalized ray theory solutions are interfaced with the finite difference calculation, and synthetics at the surface of the Earth are obtained by integrating convolutions of the output from a finite difference technique with WKB Green's functions by applying the Kirchhoff theory. Since the finite difference technique is applied in the heterogeneous region only, the hybrid method takes much less computer memory and has wide applications for high-resolution studies of localized structures. The comparisons of the hybrid method seismograms with the generalized ray theory seismograms yield good agreement.

We apply the hybrid method to study the wave propagation problem for an ultralow-velocity zone near the core-mantle boundary. Localized dome-shaped structures with a horizontal length scale of about 250 km, a vertical length scale of 40 km, a P wave velocity reduction of 10%, an S wave velocity 30%, and a density increase of 20% produce *SKS-SPdKS* waveforms which fit the most anomalous records not explainable by one-dimensional models. The general structural shape and location of the localized structure are constructed from the modeling of the data, since the complexity of waveforms is sensitive to the position of the localized structure above the core-mantle boundary, although several important issues, such as the density change and the roughness of the localized structures and the smoothness of the transition from these structures, remain unresolved due to the nature of the data. Broadband data and information from other phases are required to resolve these fine structures.

Appendix: Finite Difference Formulations in the Interfaces of Three Defined Regions

We follow the notation of *Virieux* [1986]. For the region where $n = 3$ and $m > 3$

$$
\begin{aligned}
U_{i,j}^{k+\frac{1}{2}} &= U_{i,j}^{k-\frac{1}{2}} + B_{i,j}[(\Sigma_{i+\frac{1}{2},j}^{k} - \Sigma_{i-\frac{1}{2},j}^{k}) \\
&\quad + ((\Xi_{i,j+\frac{1}{2}}^{k} + \Xi_{i,j+\frac{1}{2}}^{0,k}) - \Xi_{i,j-\frac{1}{2}}^{k})], \\
V_{i+\frac{1}{2},j+\frac{1}{2}}^{k+\frac{1}{2}} &= V_{i+\frac{1}{2},j+\frac{1}{2}}^{k-\frac{1}{2}} + B_{i+\frac{1}{2},j+\frac{1}{2}}[(\Xi_{i+1,j+\frac{1}{2}}^{k} \\
&\quad - \Xi_{i,j+\frac{1}{2}}^{k}) + (\Gamma_{i+\frac{1}{2},j+1}^{k} - (\Gamma_{i+\frac{1}{2},j}^{k} \\
&\quad - \Gamma_{i+\frac{1}{2},k}^{0,k}))], \\
\Sigma_{i+\frac{1}{2},j}^{k+1} &= \Sigma_{i+\frac{1}{2},j}^{k} + (L+2M)_{i+\frac{1}{2},j}(U_{i+1,j}^{k+\frac{1}{2}} \\
&\quad - U_{i,j}^{k+\frac{1}{2}}) + L_{i+\frac{1}{2},j}[(V_{i+\frac{1}{2},j+\frac{1}{2}}^{k+\frac{1}{2}} \\
&\quad + V_{i+\frac{1}{2},j+\frac{1}{2}}^{0,k}) - V_{i+\frac{1}{2},j-\frac{1}{2}}^{k}], \\
\Gamma_{i+\frac{1}{2},j}^{k+1} &= \Gamma_{i+\frac{1}{2},j}^{k} + L_{i+\frac{1}{2},j}(U_{i+1,j}^{k+\frac{1}{2}} - U_{i,j}^{k+\frac{1}{2}}) \\
&\quad + (L+2M)_{i+\frac{1}{2},j}[(V_{i+\frac{1}{2},j+\frac{1}{2}}^{k+\frac{1}{2}} \\
&\quad + V_{i+\frac{1}{2},j+\frac{1}{2}}^{0,k}) - V_{i+\frac{1}{2},j-\frac{1}{2}}^{k}], \\
\Xi_{i,j+\frac{1}{2}}^{k+1} &= \Xi_{i,j+\frac{1}{2}}^{k} + M_{i,j+\frac{1}{2}}[((U_{i,j+1}^{k+\frac{1}{2}} \\
&\quad - U_{i,j+1}^{0,k+\frac{1}{2}}) - U_{i,j}^{k+\frac{1}{2}}) + (V_{i+\frac{1}{2},j+\frac{1}{2}}^{k+\frac{1}{2}} \\
&\quad - V_{i-\frac{1}{2},j+\frac{1}{2}}^{k})].
\end{aligned}
$$

where k is the index of time steps, i and j are for x axis and z axis discretizations. $(U, V) = (v_x, v_z)$, $(\Sigma, \Gamma, \Xi) = (\tau_{xx}, \tau_{zz}, \tau_{xz})$, $L = \lambda \times \frac{(dt)}{(dx)}$, $M = \mu \times \frac{(dt)}{(dx)}$, and $B = \frac{(1)}{\rho} \times \frac{(dt)}{(dx)}$. dx and dt are space and time discretizations and λ, μ are Lamb's parameters. $(U^0, V^0, \Sigma^0, \Gamma^0, \Xi^0)$ are solutions for direct incident wave (I_0). Here the relationship $T = I_0 + R$ is used.

For the left boundary, $m = 3$

$$
\begin{aligned}
U^{k+\frac{1}{2}}_{i,j} &= U^{k-\frac{1}{2}}_{i,j} + B_{i,j}[((\Sigma^k_{i+\frac{1}{2},j} - \Sigma^{0,k}_{i+\frac{1}{2},j}) \\
&\quad -\Sigma^k_{i-\frac{1}{2},j}) + (\Xi^k_{i,j+\frac{1}{2}} - \Xi^k_{i,j-\frac{1}{2}})], \\
V^{k+\frac{1}{2}}_{i+\frac{1}{2},j+\frac{1}{2}} &= V^{k-\frac{1}{2}}_{i+\frac{1}{2},j+\frac{1}{2}} + B_{i+\frac{1}{2},j+\frac{1}{2}}[(\Xi^k_{i+1,j+\frac{1}{2}} \\
&\quad -(\Xi^k_{i,j+\frac{1}{2}} + \Xi^{0,k}_{i,j+\frac{1}{2}})) + (\Gamma^k_{i+\frac{1}{2},j+1} \\
&\quad -\Gamma^k_{i+\frac{1}{2},j})], \\
\Sigma^{k+1}_{i+\frac{1}{2},j} &= \Sigma^k_{i+\frac{1}{2},j} + (L+2M)_{i+\frac{1}{2},j}(U^{k+\frac{1}{2}}_{i+1,j} \\
&\quad -(U^{k+\frac{1}{2}}_{i,j} + U^{0,k+\frac{1}{2}}_{i,j})) + L_{i+\frac{1}{2},j} \\
&\quad (V^{k+\frac{1}{2}}_{i+\frac{1}{2},j+\frac{1}{2}} - V^k_{i+\frac{1}{2},j-\frac{1}{2}}), \\
\Gamma^{k+1}_{i+\frac{1}{2},j} &= \Gamma^k_{i+\frac{1}{2},j} + L_{i+\frac{1}{2},j}(U^{k+\frac{1}{2}}_{i+1,j} - (U^{k+\frac{1}{2}}_{i,j} \\
&\quad +U^{0,k+\frac{1}{2}}_{i,j})) + (L+2M)_{i+\frac{1}{2},j} \\
&\quad (V^{k+\frac{1}{2}}_{i+\frac{1}{2},j+\frac{1}{2}} - V^k_{i+\frac{1}{2},j-\frac{1}{2}}), \\
\Xi^{k+1}_{i,j+\frac{1}{2}} &= \Xi^k_{i,j+\frac{1}{2}} + M_{i,j+\frac{1}{2}}[(U^{k+\frac{1}{2}}_{i,j+1} - U^{k+\frac{1}{2}}_{i,j}) \\
&\quad +((V^{k+\frac{1}{2}}_{i+\frac{1}{2},j+\frac{1}{2}} - V^{0,k+\frac{1}{2}}_{i+\frac{1}{2},j+\frac{1}{2}}) \\
&\quad -V^k_{i-\frac{1}{2},j+\frac{1}{2}})].
\end{aligned}
$$

where $(U^0, V^0, \Sigma^0, \Gamma^0, \Xi^0)$ are solutions for whole wave field (T_0) due to one-dimensional structure for grids $n > 3$ and reflected wave field (R_0) for grids $n < 3$. Here the relationships $S = T - T_0$ and $S = R - R_0$ are used.

Special treatment is needed for the triple junction point $(m = 3, n = 3)$ of those three regions

$$
\begin{aligned}
V^{k+\frac{1}{2}}_{i+\frac{1}{2},j+\frac{1}{2}} &= V^{k-\frac{1}{2}}_{i+\frac{1}{2},j+\frac{1}{2}} + B_{i+\frac{1}{2},j+\frac{1}{2}}[(\Xi^k_{i+1,j+\frac{1}{2}} \\
&\quad -(\Xi^k_{i,j+\frac{1}{2}} + \Xi^{0,k}_{i,j+\frac{1}{2}}) + ((\Gamma^k_{i+\frac{1}{2},j+1} \\
&\quad -\Gamma^{0,k}_{i+\frac{1}{2},j+1}) - \Gamma^k_{i+\frac{1}{2},j})], \\
\Sigma^{k+1}_{i+\frac{1}{2},j} &= \Sigma^k_{i+\frac{1}{2},j} + (L+2M)_{i+\frac{1}{2},j}(U^{k+\frac{1}{2}}_{i+1,j} \\
&\quad -(U^{k+\frac{1}{2}}_{i,j} + U^{0,k+\frac{1}{2}}_{i,j})) + L_{i+\frac{1}{2},j} \\
&\quad (V^{k+\frac{1}{2}}_{i+\frac{1}{2},j+\frac{1}{2}} - (V^k_{i+\frac{1}{2},j-\frac{1}{2}} \\
&\quad +V^{0,k}_{i+\frac{1}{2},j-\frac{1}{2}})), \\
\Gamma^{k+1}_{i+\frac{1}{2},j} &= \Gamma^k_{i+\frac{1}{2},j} + L_{i+\frac{1}{2},j}(U^{k+\frac{1}{2}}_{i+1,j} - (U^{k+\frac{1}{2}}_{i,j} \\
&\quad +U^{0,k+\frac{1}{2}}_{i,j})) + (L+2M)_{i+\frac{1}{2},j} \\
&\quad (V^{k+\frac{1}{2}}_{i+\frac{1}{2},j+\frac{1}{2}} - (V^k_{i+\frac{1}{2},j-\frac{1}{2}} \\
&\quad +V^{0,k}_{i+\frac{1}{2},j-\frac{1}{2}})),
\end{aligned}
$$

where (V^0, Γ^0) are the solutions for direct wave (I_0), (U^0) is the solution of T_0, and (Ξ^0) is the solution of R_0. $\Xi^k_{3,3-\frac{1}{2}}$ can be calculated as those in $n < 3$, and $U^k_{3,3}$ can be calculated as those in $n > 3$.

Acknowledgments. We thank R. Clayton for his assistance, X. Ding for providing the WKB code and E. Garnero for providing the data. We also thank D.L. Anderson, E. Brodsky, M. Gurnis, T. Melbourne, two anonymous reviewers, and an associate editor for reviews. This work was funded by NSF grants EAR-9316441 and EAR-9629279. Contribution 6211, Division of Geological and Planetary Sciences, California Institute of Technology.

References

Alexander, S. S., and R. A. Phinney, A study of the core-mantle boundary using P waves diffracted by the Earth's core, *J. Geophys. Res.*, *71*, 5,943–5,958, 1966.

Alterman, Z. S., and F. C. Karal, Propagation of elastic waves in layered media by finite-difference methods, *Bull. Seismol. Soc. Am.*, *58*, 367–398, 1968.

Boore, D. M., Finite-difference methods for seismic wave propagation in heterogeneous materials, *Methods Comput. Phys.*, *12*, 1–37, 1972.

Chapman, C. H., Exact and approximate generalized ray theory in vertically inhomogeneous media, *Geophys. J. R. Astron. Soc.*, *46*, 201–233, 1976.

Chapman, C. H., and J. A. Orcutt, The computation of body wave synthetic seismograms in laterally homogeneous media, *Rev. Geophys.*, *23*, 105–163, 1985.

Choy, G. L., Theoretical seismograms of core phases calculated by frequency-dependent full wave theory, and their interpretation, *Geophys. J. R. Astron. Soc.*, *51*, 275–312, 1977.

Cleary, J. R., and R. A. W. Haddon, Seismic wave scattering near the core-mantle boundary: a new interpretation of precursors to PKP, *Nature*, *240*, 549–551, 1972.

Cormier, V. F., Time-domain modelling of $PKIKP$ precursors for constraints on the heterogeneity in the lowermost mantle, *Geophys. J. Int.*, *121*, 725–736, 1995.

Doornbos, D. J., Characteristics of lower mantle heterogeneities from scattered waves, *Geophys. J. R. Astron. Soc.*, *44*, 447–470, 1976.

Doornbos, D. J., On seismic wave scattering by a rough core-mantle boundary, *Geophys. J. R. Astron. Soc.*, *53*, 643–662, 1978.

Doornbos, D. J., Multiple scattering by topographic relief with application to the core-mantle boundary, *Geophys. J. Int.*, *92*, 465–478, 1988.

Dziewonski, A., and D. L. Anderson, Preliminary reference Earth model, *Phys. Earth Planet. Inter.*, *25*, 297–356, 1981.

Emmerich, H., 2-D wave propagation by a hybrid method, *Geophys. J. Int.*, *99*, 307–319, 1989.

Garnero, E. J., and D. V. Helmberger, A very slow basal layer underlying large-scale low-velocity anomalies in the lower mantle beneath the Pacific: Evidence from core phases, *Phys. Earth Planet. Inter.*, *91*, 161–176, 1995.

Garnero, E. J., and D. V. Helmberger, Seismic detection of a thin laterally varying boundary layer at the base of the mantle beneath the central-Pacific, *Geophys. Res. Lett.*, *23*, 977–980, 1996.

Garnero, E. J., and D. V. Helmberger, Further structural-constraints and uncertainties of a thin laterally varying ultralow velocity layer at the base of the mantle, *J. Geophys. Res.*, *in press*, 1998.

Garnero, E. J., S. P. Grand, and D. V. Helmberger, Low P-wave velocity at the base of the mantle, *Geophys. Res. Lett.*, *23*, 977–980, 1993.

Helmberger, D. V., The crust-mantle transition in the Bering Sea, *Bull. Seismol. Soc. Am.*, *58*, 179–214, 1968.

Helmberger, D. V., Theory and application of synthetic seismograms, in *Earthquakes: Observation, Theory and In-*

terpretation, edited by H. Kanamori, pp. 173–222, Soc. Ital. di Fis., Bologna, Italy, 1983.

Helmberger, D. V., E. J. Garnero, and X. Ding, Modeling two-dimensional structure at the core-mantle boundary, *J. Geophys. Res.*, *101*, 13,963–13,972, 1996.

Hong, T. L., and D. V. Helmberger, Glorified optics and wave propagation in nonplanar structure, *Bull. Seismol. Soc. Am.*, *68*, 1313–1330, 1978.

Igel, H., and M. Weber, $P-SV$ wave propagation in the Earth's mantle using finite-difference: Application to heterogeneous lowermost mantle structure, *Geophys. Res. Lett.*, *23*, 415–418, 1996.

Levander, A. R., Fourth-order finite-difference $P-SV$ seismograms, *Geophysics*, *53*, 1425–1436, 1988.

Liu, X. F., and J. Tromp, Uniformly valid body-wave ray theory, *Geophys. J. Int.*, *127*, 461–491, 1996.

Lysmer, J., and L. A. Drake, A finite element method for seismology, *Methods Comput. Phys.*, *11*, 181–216, 1972.

Mori, J., and D. V. Helmberger, Localized boundary layer below the mid-Pacific velocity anomaly identified from *PcP* precursor, *J. Geophys. Res.*, *100*, 20,359–20,365, 1995.

Müller, G., The reflectivity method: A tutorial, *J. Geophys.*, *58*, 153–174, 1985.

Shtivelman, V., Two-dimensional acoustic modeling by a hybrid method, *Geophysics*, *50*, 1273–1284, 1985.

Stead, R. J., and D. V. Helmberger, Numerical-analytical interfacing in two dimensions with applications to modeling NTS seismograms, *Pure Appl. Geophys.*, *128*, 153–174, 1988.

Vidale, J. E., and M. Hedlin, Evidence for partial melt at the core-mantle boundary north of Tonga from the strong scattering of seismic-waves, *Nature*, *391*, 682–684, 1998.

Virieux, J., *SH*-wave propagation in heterogeneous media: Velocity-stress finite-difference method, *Geophysics*, *49*, 1,933–1,957, 1984.

Virieux, J., $P-SV$ wave propagation in heterogeneous media: Velocity-stress finite-difference method, *Geophysics*, *51*, 889–901, 1986.

Wen, L., and D. V. Helmberger, Ultra low velocity zones near the core-mantle boundary from broadband *PKP* precursors, *Science*, *279*, 1701–1703, 1998.

Williams, Q., and E. J. Garnero, Seismic evidence for partial melt at the base of Earth's mantle, *Science*, *273*, 1,528–1,530, 1996.

D. V. Helmberger and L. Wen, Seismological Laboratory, California Institute of Technology 252-21, Pasadena, CA 91125. (e-mail: wen@gps.caltech.edu)

(Received July 23, 1997; revised January 15, 1998; accepted April 9, 1998.)